CHAPTER III

Experimental Techniques

3.1 Materials

Graphite powder from Loba Chemie, potassium permanganate ($KMnO_4$) and hydrogen peroxide (H_2O_2, 30%) from Merck, concentrated sulphuric acid (H_2SO_4, 98%), phosphoric acid (H_3PO_4, 98%) and hydrochloric acid (HCl, 36%) from Rankem, India were procured for the synthesis of graphite oxide. The reducing agent hydrazine hydrate ($N_2H_4.H_2O$, 80%) was purchased from Sisco Research Laboratory (SRL). The monomer 3, 4-ethylenedioxythiophene (EDOT ≥ 97%) and dopant Poly (4-styrenesulfonic acid) (PSS, M_w=75,000 g mol^{-1}) were procured from Sigma Aldrich. The oxidizing agents ferric chloride ($FeCl_3$, purity ≥97%) and ammonium peroxydisulfate [$(NH_4)_2S_2O_8$, purity ≥98%] used in polymerization process were supplied from Sigma Aldrich and Merck, respectively. The metal precursors nickel nitrate hexahydrate [$Ni(NO_3)_2.6H_2O$, 99%], manganese (II) chloride tetrahydrate ($MnCl_2.4H_2O$, 99%) and nickel (II) chloride hexahydrate ($NiCl_2.6H_2O$, 98%) were obtained from Merck and Sisco Research Laboratories respectively. The oxalic acid [$(COOH)_2.2H_2O$, 99%] and sodium hydroxide (NaOH) were procured from Fisher Scientific and Merck, respectively. The solvents methanol (CH_3OH, 99%), ethanol (C_2H_5OH, 99%) and acetone $(CH_3)_2CO$ were purchased from Merck. Indium tin oxide (ITO) glasses were obtained from Macwin, India for fabrication of electrodes. All the chemicals were analytical grade reagent and used without further purification. Deionized water (DI water) from Milli-Q plus system was used during the experiments. The physical properties of the materials used for the synthesis of metal oxides, rGO, PEDOT:PSS and their nanocomposites in the present work are presented in Table 3.1.

Table 3.1: *Some physical properties of the materials used in synthesis.*

Physical properties of monomer

Monomer	Molecular formula	Molecular weight (gm mol^{-1})	Melting point (°C)	Boiling point (°C)	Density at 25°C (gm ml^{-1})	Oxidation potential (V)
3, 4-Ethylenedioxythiophene (EDOT)	$C_6H_6O_2S$	142.18	10-11	193	1.331	1.2 Vs. Ag/AgCl

Physical properties of oxidant

Oxidant	Molecular formula	Molecular weight (gm mol^{-1})	Melting point (°C)	Boiling point (°C)	Density at 25°C (gm ml^{-1})
Ferric chloride	$FeCl_3$	162.2	306	315	2.898
Ammonium peroxydisulfate	$(NH_4)_2S_2O_8$	228.18	120	-	1.98

Physical properties of metal precursors

Metal precursor	Molecular formula	Molecular weight (gm mol^{-1})	Melting point (°C)	Boiling point (°C)	Density at 25°C (gm ml^{-1})
Nickel nitrate hexahydrate	$Ni(NO_3)_2.6H_2O$	290.81	56	136	2.05
Manganese (II) chloride tetrahydrate	$MnCl_2.4H_2O$	197.90	58	-	2.01
Nickel (II) chloride hexahydrate	$NiCl_2.6H_2O$	237.69	140	-	1.92

Physical properties of solvents and acids

Solvent	Molecular formula	Molecular weight (gm mol^{-1})	Melting point (°C)	Boiling point (°C)	Density (gm ml^{-1})
Acetone	C_3H_6O	58.08	-95	56	0.791
Methanol	CH_4O	32.04	-97.6	64.7	0.791
Ethanol	C_2H_6O	46.06	-114	78.37	0.789
Sulphuric acid	H_2SO_4	98.08	10	337	1.84
Phosphoric acid	H_3PO_4	97.99	40-42.4	212	1.68
Hydrochloric acid	HCl	36.46	-30	61	1.18
Oxalic acid	$(COOH)_2.2H_2O$	126.07	101-105	149 - 160	1.65

Physical properties of other chemicals used in synthesis process

Chemical	Molecular formula	Molecular Weight (gm mol^{-1})	Melting point (°C)	Boiling point (°C)	Density (gm ml^{-1})
Graphite	C	12.01	3652-3697	-	2.09-2.23
Potassium permanganate	$KMnO_4$	158.03	240	-	2.70
Hydrogen peroxide	H_2O_2	34.01	-0.43	150.2	1.11
Hydrazine hydrate	$NH_2NH_2.H_2O$	50.06	-51.7	120.1	1.02
Poly (4-styrenesulfonic acid)	$(C_8H_8O_3S)_n$	75,000	-	-	1.11
Sodium hydroxide	NaOH	40	318	1388	2.13

3.2 Synthesis of reduced graphene oxide (rGO), PEDOT:PSS and manganese dioxide (MnO_2) nanorod based ternary nanocomposite

3.2.1 Synthesis of graphite oxide (GO)

Graphite oxide (GO) was synthesized using Improved Hummers' method [1]. In this method, graphite powder was oxidized in presence of concentrated H_2SO_4 and H_3PO_4 using $KMnO_4$ as oxidizing agent. Initially, 3 g of graphite powder was added to a mixture of 360 ml concentrated H_2SO_4 and 40 ml H_3PO_4 and stirred for 1 h. After that, 18 g $KMnO_4$ was slowly added to the mixture under constant stirring maintaining the temperature below 30 °C by keeping the beaker in a water bath. Then, the solution was stirred at 60 °C for 12 h resulting into a brown coloured mixture indicating successful reaction. Subsequently, ice formed out of 400 ml of DI water was added, followed by mixing of 70 ml of 30% H_2O_2 solution into the mixture. The bright yellow reaction mixture was centrifuged at a speed of 500-1000 rpm for 30 min, and the supernatant part containing unoxidized graphite and impurities was decanted slowly. The as obtained precipitate was washed repeatedly with DI water, absolute ethanol and 5% HCl solution in sequence to make the pH neutral. Thereafter, the resultant product was dried at room

temperature to obtain GO. The block diagram showing the synthesis process of GO is presented in Figure 3.1.

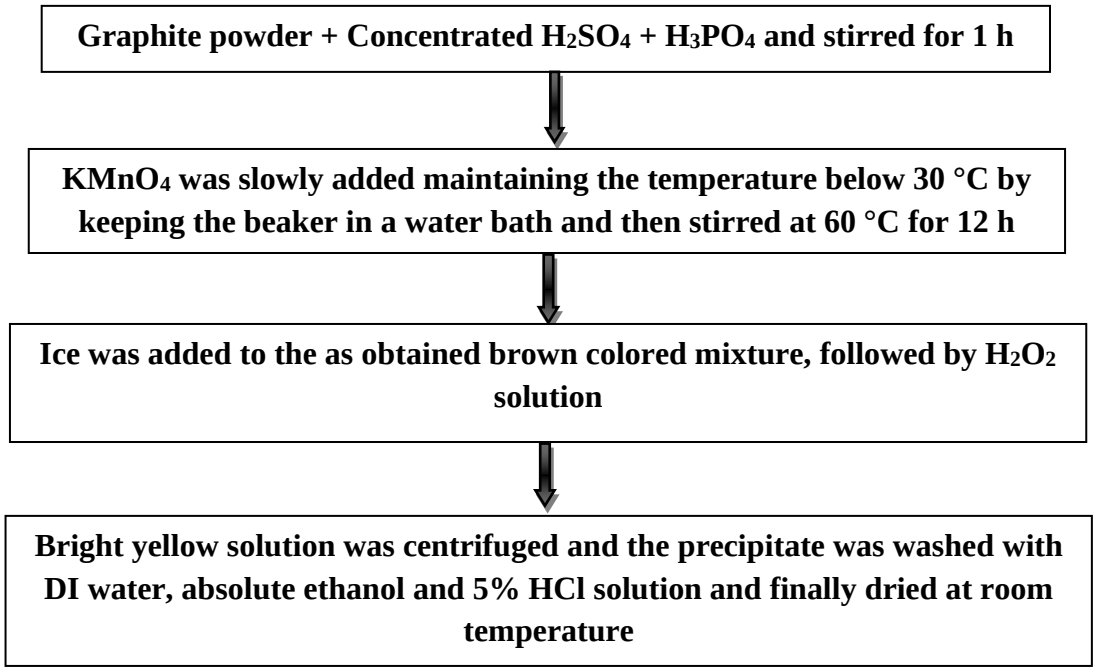

Figure 3.1: *Block diagram of synthesis of GO via Improved Hummers' method.*

3.2.2 Synthesis of α-MnO_2 nanorods

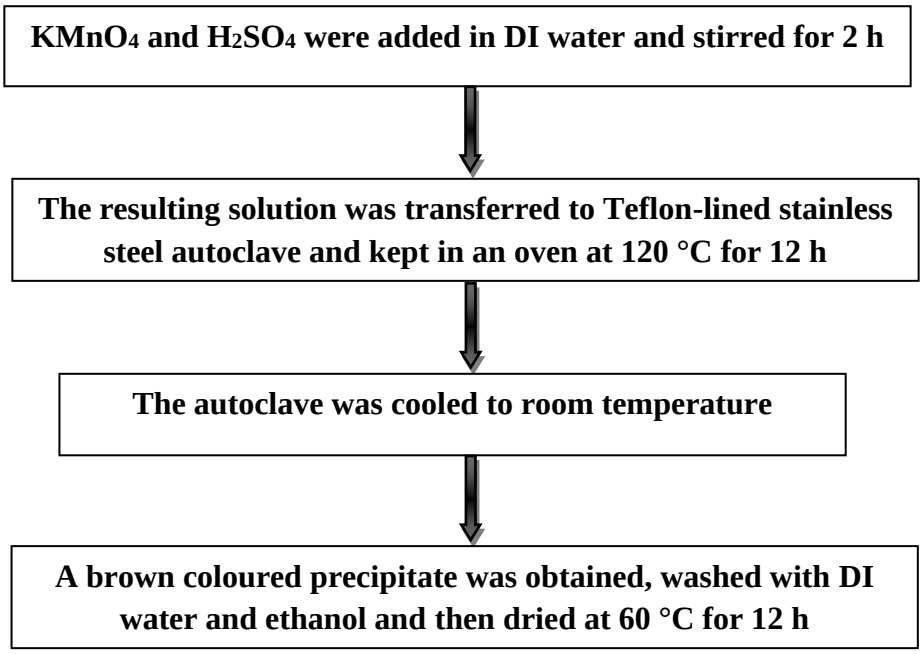

Figure 3.2: *Block diagram of synthesis of α- MnO_2 nanorods.*

α-MnO_2 nanorods were synthesized via hydrothermal route [2]. In this procedure, 0.6 g $KMnO_4$ and 0.4 ml H_2SO_4 were added in 50 ml DI water under constant stirring for 2 h. Then the resulting solution was transferred to Teflon-lined stainless steel autoclave and kept in an oven at 120 °C for 12 h. Then the autoclave was cooled to room temperature and the product obtained was repeatedly washed with DI water and ethanol to remove the unreacted part. The precipitated MnO_2 was dried in an oven at 60 °C for 12 h. The block diagram for the synthesis of α- MnO_2 nanorods are shown in Figure 3.2.

3.2.2.1 Formation mechanism of α-MnO_2 nanorods

In acidic medium $KMnO_4$ is unstable, hence it decomposes into MnO_2 and O_2 [3]. Under hydrothermal condition, the rate of decomposition increases significantly resulting into large amount of MnO_2 colloids. Due to large concentration and surface energies, the MnO_2 colloids tend to agglomerate. Under optimized conditions, the minor colloids grow and form small nanorods due to their tendency of 1D growth. Gradually, the reaction rate decreases due to consumption of reactants. The whole process gains thermodynamic stability after complete consumption of $KMnO_4$. In this reaction, the small nanorods grow into larger ones due to energy differences among them and the process is known Ostwald ripening mechanism. The growth of MnO_2 nanorods follows the reaction given below [2]:

$$4MnO_4^- + 2H_2O \rightarrow 4MnO_2 + 4OH^- + 3O_2 \qquad [3.1]$$

3.2.3 Synthesis of PEDOT:PSS/MnO_2 nanocomposite

PEDOT:PSS/MnO_2 nanocomposite was synthesized via *in-situ* polymerization using EDOT monomer. The typical procedure is explained as follows: 50 mg of as-synthesized MnO_2 nanorods were added in 100 ml of DI water and ultrasonicated for 2 h. The solution was taken out from ultrasonication for polymerization. 115 µl of PSS and 37 µl of EDOT were added to the above solution and kept for stirring. Subsequently 30 ml solution containing 0.342 g of ammonium peroxydisulfate and 0.243 g of ferric chloride was added to the solution. The above mixture was kept in an ice bath for 24 h for successful polymerization. Finally the resultant nanocomposite was centrifuged with DI water and ethanol to remove the unreacted part and then dried overnight at 60 °C. The block diagram for the synthesis of PEDOT:PSS/MnO_2 nanocomposite is shown in Figure 3.3.

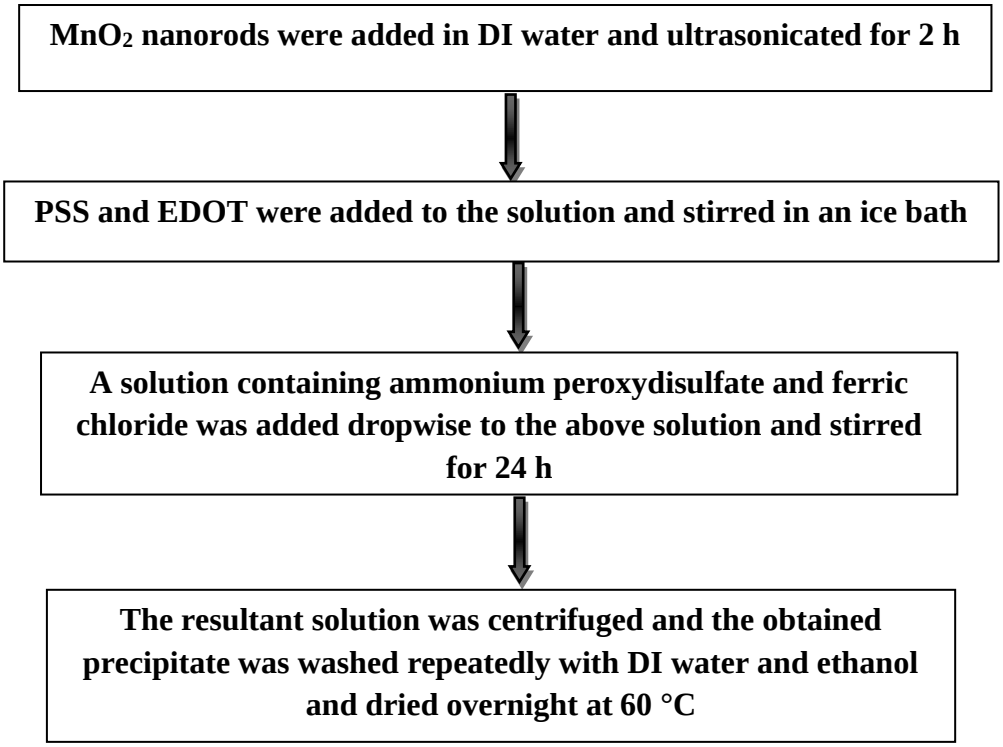

Figure 3.3: *Block diagram of synthesis of PEDOT:PSS/MnO_2 nanocomposite.*

3.2.4 Synthesis of rGO/PEDOT:PSS/MnO_2 nanocomposite

The rGO/PEDOT:PSS/MnO_2 nanocomposite was synthesized via *in-situ* polymerization using EDOT monomer. The typical procedure is explained as follows: the as-synthesized GO was dispersed in DI water with concentration 2 mg ml^{-1} by ultrasonication for 2 h to obtain homogeneous solution. The dispersion of GO solution was chemically reduced using hydrazine hydrate (4 µl ml^{-1}) at 95 °C to form rGO. The obtained rGO solution was cooled to room temperature. 50 mg of MnO_2 nanorods were added to the solution and ultrasonicated for 2 h. The solution was taken out from ultrasonication for polymerization. 115 µl of PSS and 37 µl of EDOT were added to the above solution and kept for stirring, and then 30 ml solution containing 0.342 g of ammonium peroxydisulfate and 0.243 g of ferric chloride was added to the solution. The above mixture was kept in an ice bath for 24 h for successful polymerization. Finally the resultant nanocomposite was centrifuged with DI water and ethanol to remove the unreacted part and then dried overnight at 60 °C. The block diagram for the synthesis of PEDOT:PSS/MnO_2 nanocomposite is shown in Figure 3.4.

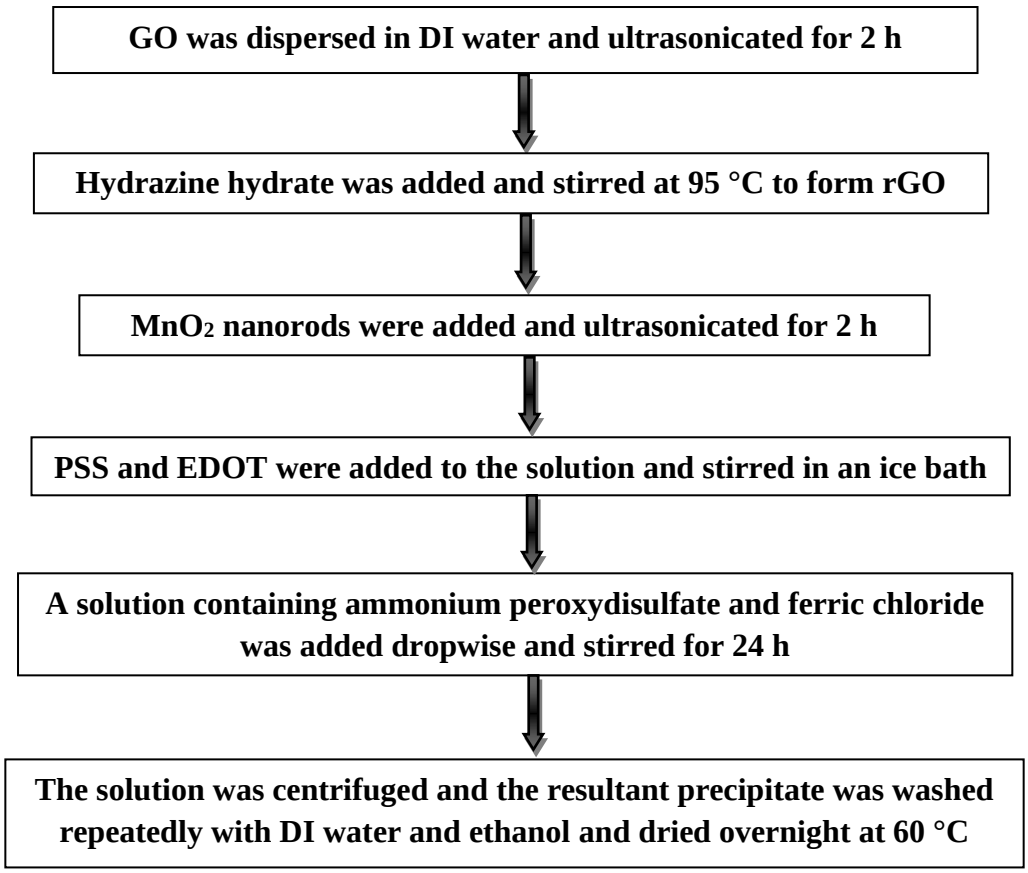

Figure 3.4: *Block diagram of synthesis of rGO/PEDOT:PSS/MnO_2 nanocomposite.*

3.2.4.1 Formation mechanism of rGO/PEDOT:PSS/MnO_2 nanocomposite

Schematic illustration of formation of rGO/PEDOT:PSS/MnO_2 ternary nanocomposite is shown in Figure 3.5. Initially GO is reduced to rGO using hydrazine hydrate as reducing agent. The MnO_2 nanorods are assembled on rGO nanosheets and then coated by *in situ* polymerized PEDOT:PSS [4]. As-synthesized rGO contains many oxygen containing functional (epoxy, carboxyl, hydroxyl) groups which act as active sites for the attachment of EDOT and MnO_2 nanorods [2]. The monomer adsorbed on rGO sheet starts to polymerize on addition of APS and $FeCl_3$. In this process, MnO_2 nanorod, APS and $FeCl_3$ behave as oxidizing agents for polymerization. Although the redox potential of Fe^{3+}/Fe^{2+} (equation 3.2) is lower than MnO_2/Mn^{2+} (equation 3.3), but the higher redox potential of $S_2O_8^{2-}/SO_4^{2-}$ (equation 3.4) initiates the polymerization inhibiting the consumption of MnO_2 nanorods to form the ternary nanocomposite [5].

$$Fe^{3+} + e^- \leftrightarrow Fe^{2+} \qquad E^0 = +0.771\ V \qquad [3.2]$$

$$MnO_2 + 4H^+ + 2e^- \leftrightarrow Mn^{2+} + 4H_2O \qquad E^0 = +1.23\ V \qquad [3.3]$$

$$S_2O_8^{2-} + 2e^- \leftrightarrow 2SO_4^{2-} \qquad E^0 = +2.010\ V \qquad [3.4]$$

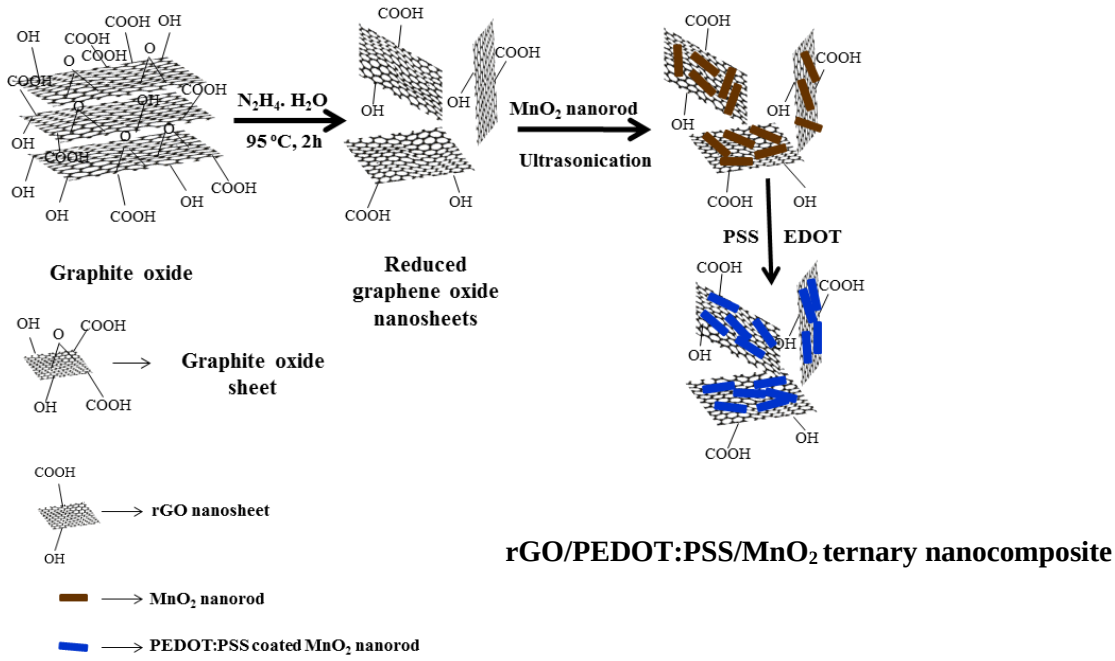

Figure 3.5: *Schematic representation of formation of rGO/PEDOT:PSS/MnO_2 ternary nanocomposite.*

3.3 Synthesis of reduced graphene oxide (rGO), PEDOT:PSS and nickel oxide (NiO) based ternary nanocomposite

3.3.1 Synthesis of NiO nanoplate-nanorod structure

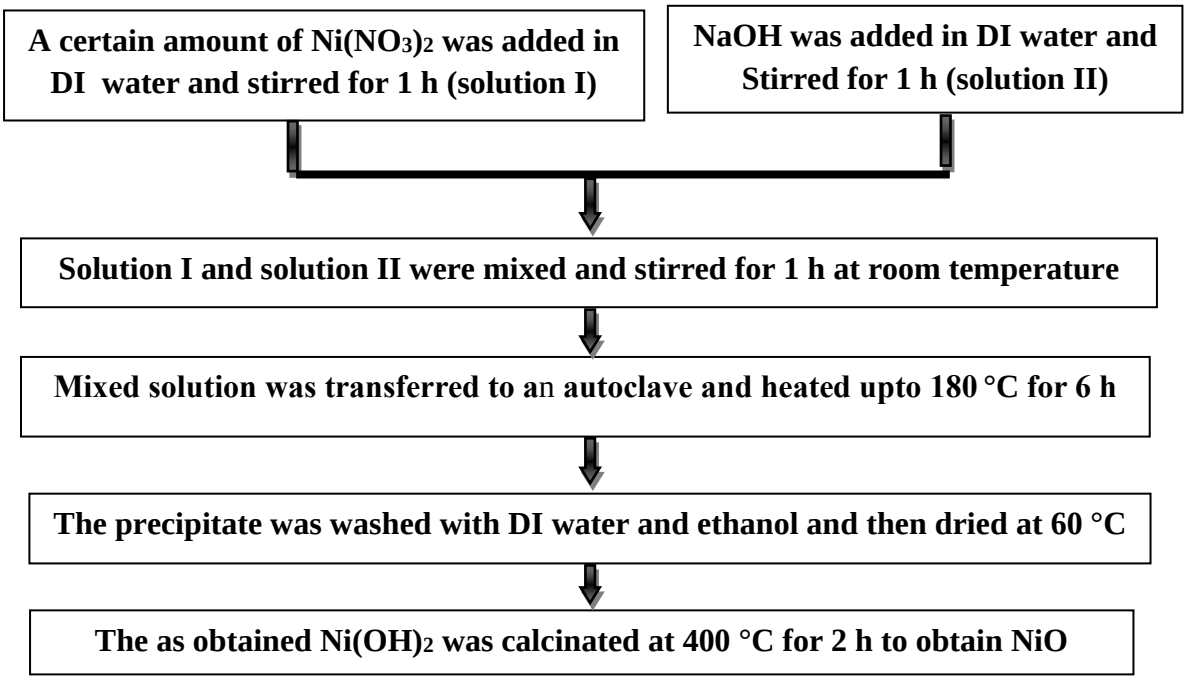

Figure 3.6: *Block diagram of synthesis of NiO nanoplate-nanorod structure.*

Initially $Ni(OH)_2$, a precursor was prepared via hydrothermal route, then calcination was done to transform $Ni(OH)_2$ into NiO nanoplate-nanorod hybrid. In this typical method, to prepare $Ni(OH)_2$, two solutions termed as solution I containing $Ni(NO_3)_2$ in DI water and solution II containing NaOH in DI water were prepared, keeping the ratio between $Ni(NO_3)_2$ and NaOH as 1:8. Next, a homogeneous solution was prepared by continuous mixing and stirring of solution I and solution II at room temperature for 1 h. After that, the mixture solution was heated at 180 °C for 6 h in a Teflon-lined steel autoclave and then cooled to room temperature. The resulting green coloured precipitate was centrifuged several times with ethanol and DI water before being dried in a vacuum oven at 60 °C to obtain $Ni(OH)_2$. After that, the as obtained $Ni(OH)_2$ was calcinated in a furnace at 400 °C for 2 h to form black coloured NiO powder. The block diagram of synthesis of NiO nanoplate-nanorod structure is shown in Figure 3.6.

3.3.1.1 Formation mechanism of NiO nanoplate-nanorod structure

$Ni(NO_3)_2.6H_2O$ dissociates into Ni^{2+} cations and NO_3^{2-} anions in water as shown in equation 3.5. Similarly, NaOH dissociates into Na^+ cations and OH^- anions in water as presented in equation 3.6 [6].

$$Ni(NO_3)_2 \rightarrow Ni^{2+} + NO_3^{2-} \quad [3.5]$$

$$NaOH \rightarrow Na^+ + OH^- \quad [3.6]$$

The Ni^{2+} cations and OH^- anions react with each other forming into $Ni(OH)_2$ nuclei as presented in equation 3.7.

$$Ni^{2+} + 2OH^- \rightarrow Ni(OH)_2 \quad [3.7]$$

In the process of formation of NiO, initially nucleation of small nanoparticles of precursor occurs due to hydrolysis of $Ni(NO_3)_2$ and NaOH in water at a ratio 1:8 [7]. Various factors including electrostatic force, Van der Waals interaction, hydrogen bonding, crystal face attraction, hydrophobic interaction, and Ostwald ripening contribute during the reaction. After attaining a critical size, the nuclei grow further to lower interfacial surface free energy. Nuclei gain stability as they start growing and exceed the critical nuclei size. The developed material exhibits both 1D and 2D nanostructures (nanorods and nanoplates) depending upon the time of hydrothermal reaction. Usually, uniform $Ni(OH)_2$ nanoparticles grow and gradually transform into 1D nanorods. However, the larger concentration of NaOH as compared to $Ni(NO_3)_2$, attributes to the decrease in length of 1D nanostructure. The excess amount of OH^- anions present in the system inhibit

intercalation of other species into the as-formed nuclei, along with strong steric effect resulting into formation of $Ni(OH)_2$ nanoplates [8]. Thus, these nanorods started to convert into nanoplates due to longer reaction time [9]. Although due to optimized reaction conditions, considerable amount of NiO nanorods also exist along with nanoplates. Upon calcination at 400 ^oC, the hexagonal $Ni(OH)_2$ has been transformed into porous hexagonal NiO nanoplates by losing water molecules. Finally, NiO is formed upon annealing of $Ni(OH)_2$ at an elevated temperature.

$$Ni(OH)_2 \xrightarrow{\text{annealed at 400 °C}} NiO + H_2O \text{ vapour} \qquad [3.8]$$

3.3.2 Synthesis of PEDOT:PSS/NiO nanocomposite

The PEDOT:PSS/NiO nanocomposite was synthesized via *in-situ* polymerization method. Initially, 50 mg of NiO was incorporated into 100 ml of DI water and ultrasonicated for 2 h. Then 37 µl of monomer (EDOT) was added into the above solution followed by 115 µl of PSS. Subsequently, 0.342 g of ammonium peroxydisulfate and 0.243 g of ferric chloride dissolved in 30 ml of DI water was added drop wise into the solution. For successful polymerization, the solution mixture was kept in an ice bath for 24 h. The resulting solution was centrifuged and washed with DI water and ethanol and finally dried at 60 ^oC to obtain PEDOT:PSS/NiO nanocomposite. The block diagram for the synthesis of PEDOT:PSS/NiO nanocomposite is shown in Figure 3.7.

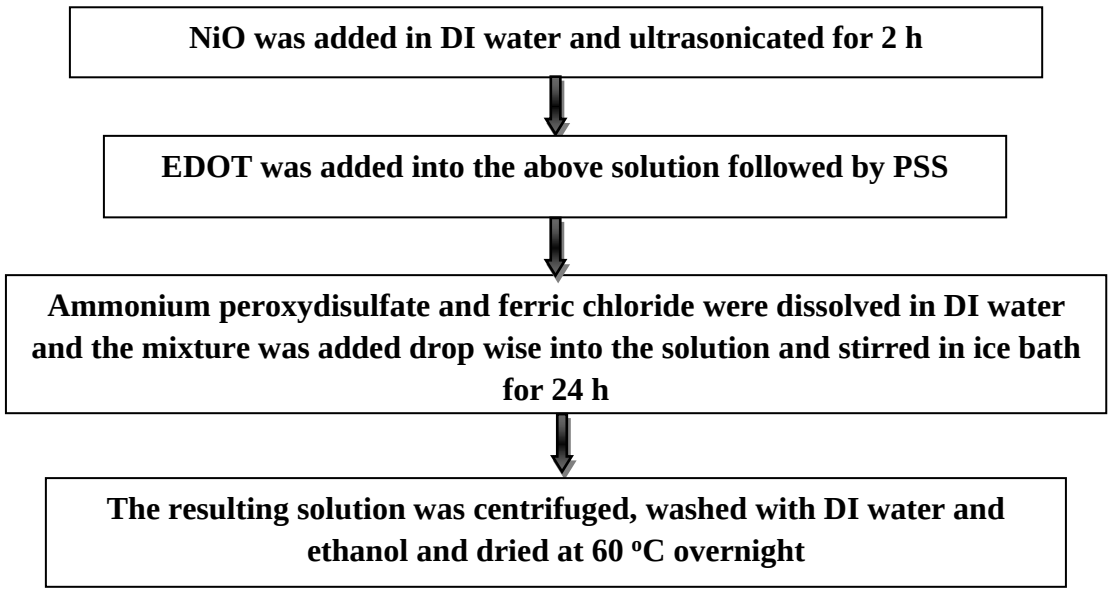

Figure 3.7: *Block diagram of synthesis of PEDOT:PSS/NiO nanocomposite.*

3.3.3 Synthesis of rGO/PEDOT:PSS/NiO nanocomposite

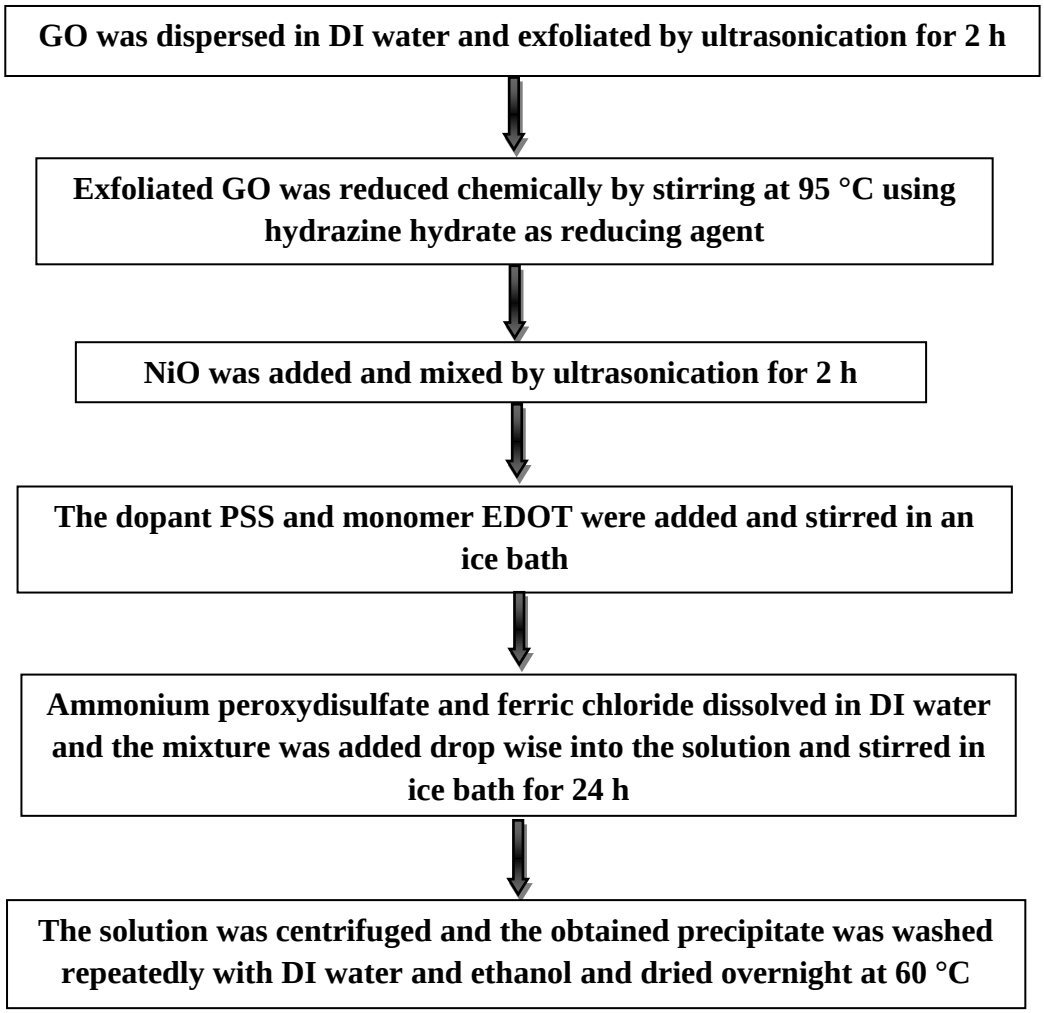

Figure 3.8: *Block diagram of synthesis of rGO/PEDOT:PSS/NiO nanocomposite.*

rGO/PEDOT:PSS/NiO nanocomposite was prepared using *in-situ* polymerization technique, where Improved Hummers' method was employed to synthesize Graphite oxide (GO) [10]. Here, the exfoliation of GO was carried out by dissolving 2 mg of GO in per ml of DI water and sonication for 2 h. After that, 4 µl of hydrazine hydrate was added to per ml of exfoliated GO solution and stirred continuously at 95 °C until rGO is formed. Subsequently, 50 mg of NiO was added to the above solution and sonicated for 2h. Then polymerization was done in presence of 37 µl of monomer EDOT and 115 µl of dopant PSS under constant stirring in ice bath. During polymerization, 0.342 g of ammonium peroxydisulfate and 0.243 g of ferric chloride dissolved in 30 ml of DI water were slowly mixed to this above solution and stirred in an ice bath for 24 h. The formation of blue coloured solution suggests that EDOT monomer was successfully polymerized to PEDOT

in presence of NiO and rGO. The as obtained precipitate was repeatedly washed with ethanol and DI water and finally dried at 60 °C in a vacuum oven. The block diagram for the synthesis of rGO/PEDOT:PSS/NiO nanocomposite is shown in Figure 3.8.

3.3.3.1 Formation mechanism of rGO/PEDOT:PSS/NiO nanocomposite

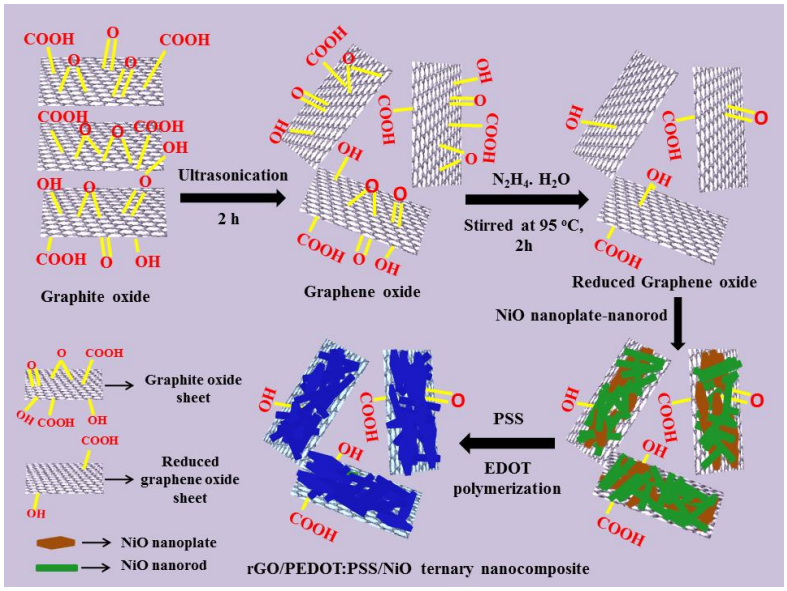

Figure 3.9: *Schematic illustration of formation of rGO/PEDOT:PSS/NiO ternary nanocomposite.*

The preparation process of rGO/PEDOT:PSS/NiO nanocomposite is presented in Figure 3.9. According to Improved Hummer's method [43], graphite oxidizes to graphite oxide having large interlayer spacing and large number of oxygenated groups. Then graphite oxide has been exfoliated and reduced using hydrazine hydrate to form rGO sheets. On the other hand, a layer of EDOT and PSS has been formed around NiO upon chemical treatment owing to the interaction between NiO and EDOT. However, the interaction between NiO and EDOT is weak because of metallic nature of NiO. Thus, partial destabilization of EDOT molecules leads to the formation of nucleation centre and further, incorporation of oxidizing agent oxidizes it and forms PEDOT:PSS coated nanocomposite. Usually, there is strong π-π interaction between the conjugated structure of PEDOT:PSS and the basal plane of graphitic surface through EDOT ring. Large amount of active area is accessible in rGO-PEDOT:PSS nanocomposite for dispersion of NiO.

3.4. Synthesis of reduced graphene oxide (rGO), PEDOT:PSS and nickel manganese spinel oxide ($NiMn_2O_4$) based ternary nanocomposite

3.4.1 Synthesis of $NiMn_2O_4$ nanoparticles

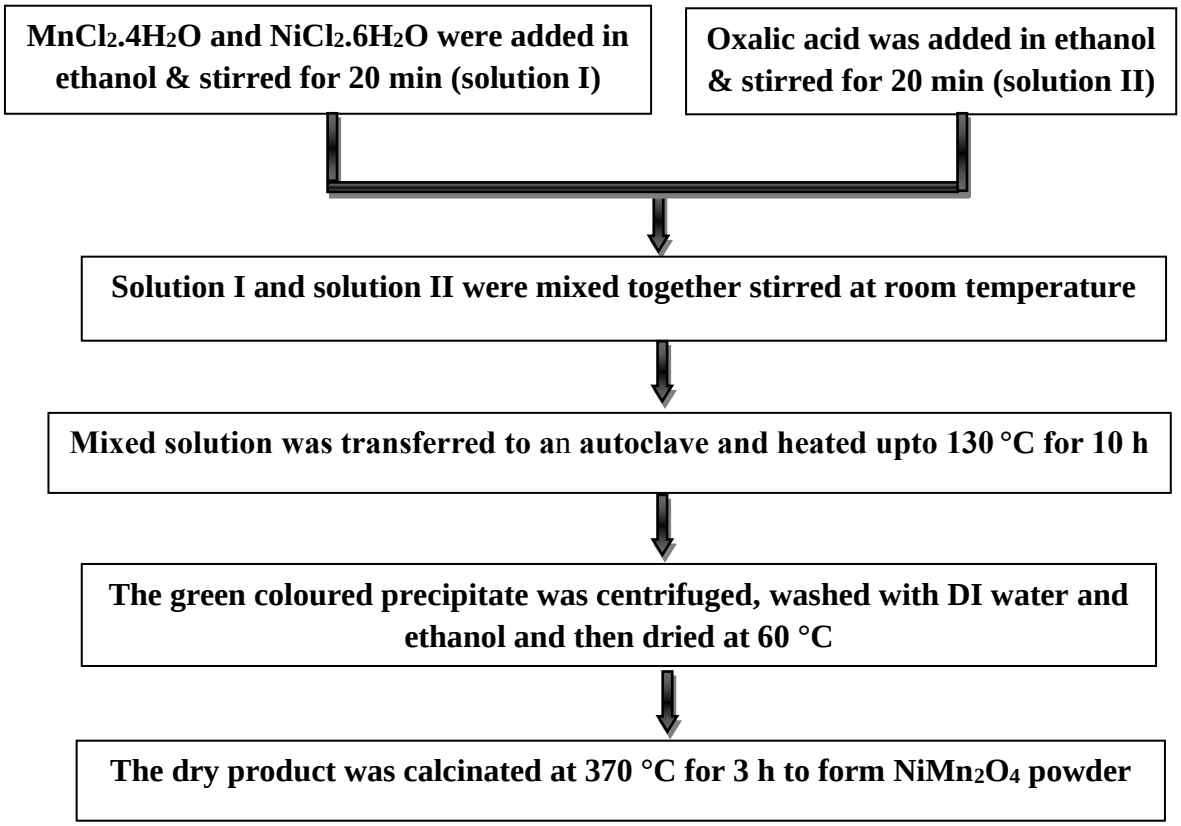

***Figure 3.10**: Block diagram of synthesis of $NiMn_2O_4$ nanoparticles.*

The nickel-manganese precursor nanoparticles were initially prepared by solvothermal process. In this typical process, 2 g of $MnCl_2.4H_2O$ and 1 g of $NiCl_2.6H_2O$ were dissolved in 50 ml of ethanol and stirred for 20 min and named as solution I; simultaneously, 1.51 g of oxalic acid solution in 20 ml of ethanol, named as solution II was stirred for 20 min. After that, solution I and solution II were mixed together and continuously stirred at room temperature and a homogeneous solution was formed and then the mixture was transferred to a Teflon-lined steel autoclave. After sealing, the autoclave was kept at a temperature of 130 °C for 10 h. After completion of the reaction, the green coloured precipitate was centrifuged and washed several times with DI water and ethanol and dried at 60 °C. The dry product was calcinated at 370 °C for 3 h to form $NiMn_2O_4$ powder. The

block diagram for the synthesis of PEDOT:PSS/NiO nanocomposite is shown in Figure 3.10.

3.4.1.1 Formation mechanism of $NiMn_2O_4$ nanoparticles

To synthesize $NiMn_2O_4$ nanoparticles, the precursor materials $NiCl_2$ and $MnCl_2$ (weight ratio 1:2) have been hydrolysed in ethanol solution that follows by addition of oxalic acid to control the morphology of nanoparticles. Then Ni-Mn hydroxide nanoparticles have been formed due to solvothermal treatment of the above mentioned precursor solution at 130 °C for 10 h. Under solvothermal process, the precursor materials nucleate and form granular particle like structures. This reaction process depends on numerous factors such as van der Waals forces, intrinsic crystal contraction, crystal face attraction, Ostwald ripening, hydrogen bonding, electrostatic and dipolar fields and hydrophobic interaction etc. [11]. Finally, the Ni-Mn hydroxide nanoparticles are transformed into $NiMn_2O_4$ nanoparticles during calcination at 370 °C in presence of air. The formation process of $NiMn_2O_4$ nanoparticles can be explained according to the reported work by Rui Ding et al. [12]. During calcination process, initially, Ni-Mn hydroxide primary nanoparticles are sintered with each other to form the irregular shaped secondary particles and finally, the secondary Ni-Mn hydroxide nanoparticles start to sinter and increase in size. In the calcinations process, the fine Ni-Mn hydroxide primary nanoparticles aggregate with simultaneous release of gases, and thus forming the granular porous structures. The porous structure of materials boosts the ion transfer between the anode material and electrolyte interface, which is considered to be one of the important factors for enhancement in electrochemical activities of the catalysts.

3.4.2 Synthesis of PEDOT:PSS/$NiMn_2O_4$ nanocomposite

In-situ polymerization technique was employed to synthesize PEDOT:PSS/$NiMn_2O_4$ nanocomposite. In this process, 50 mg of $NiMn_2O_4$ was mixed in 100 ml of DI water by ultrasonication for 2 h. After that, 37 µl of monomer (EDOT) and 115 µl of PSS were added into the above solution, followed by drop wise addition of a mixture solution of 0.342 g of ammonium peroxydisulfate and 0.243 g of ferric chloride dissolved in 30 ml of DI water. The polymerization was performed by keeping the solution mixture in an ice bath for 24 h. The resulting solution was centrifuged and washed with DI water and ethanol and finally dried at 60 ^oC to obtain PEDOT:PSS/$NiMn_2O_4$ nanocomposite. The block diagram for the synthesis of PEDOT:PSS/$NiMn_2O_4$ nanocomposite is shown in Figure 3.11.

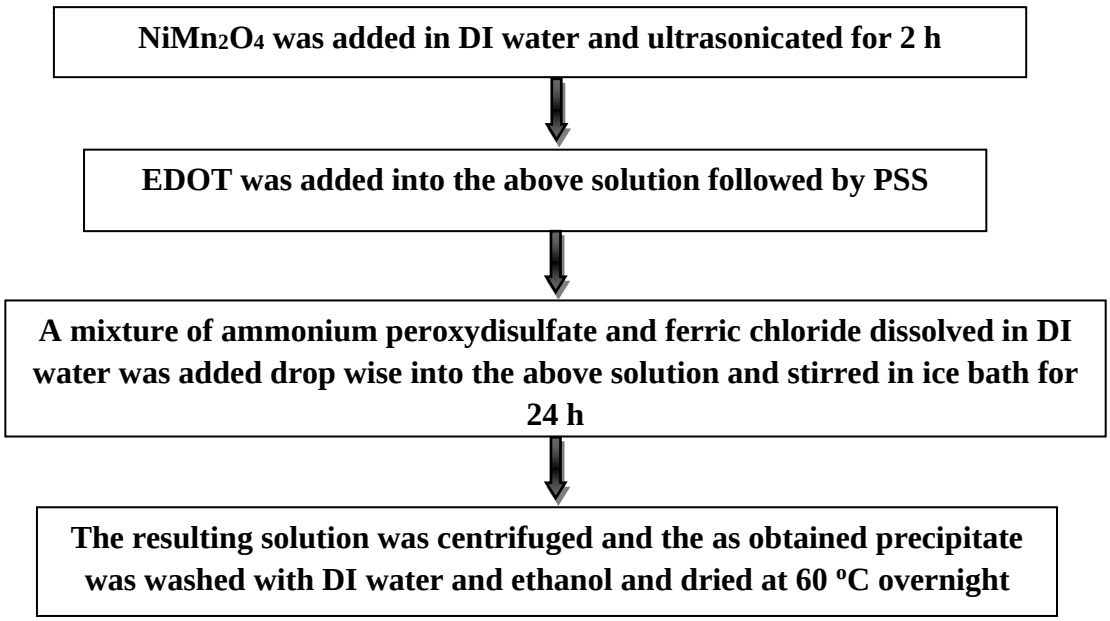

Figure 3.11: *Block diagram of synthesis of PEDOT:PSS/$NiMn_2O_4$ nanocomposite.*

3.4.3 Synthesis of rGO/PEDOT:PSS/$NiMn_2O_4$ nanocomposite

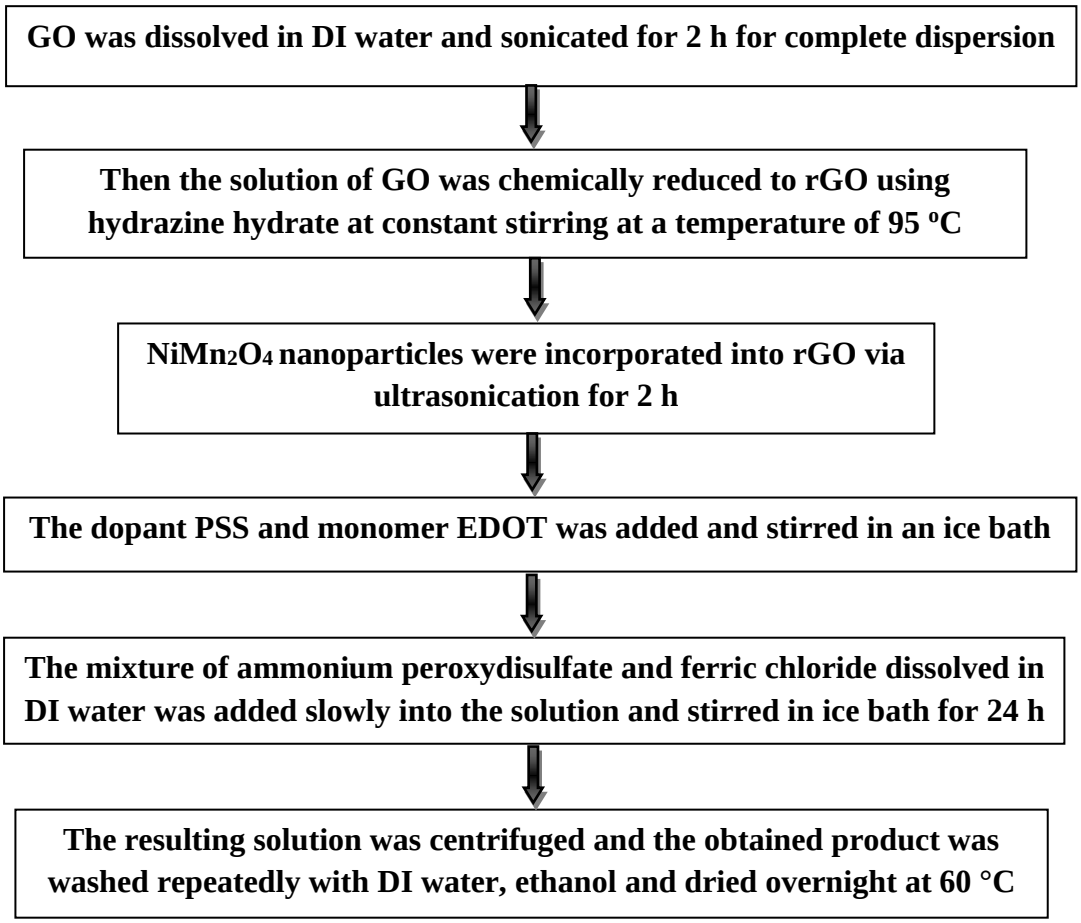

Figure 3.12: *Block diagram of synthesis of rGO/PEDOT:PSS/$NiMn_2O_4$ nanocomposite.*

Graphite oxide (GO) was prepared via Improved Hummers' method as mentioned in literature [1]. rGO/PEDOT:PSS/$NiMn_2O_4$ nanocomposite was synthesized via *in situ* polymerization of EDOT monomers. In this typical method, 2 mg ml^{-1} of GO was dissolved in DI water and sonicated for 2 h for complete dispersion of GO. Then the solution of GO was chemically reduced to rGO using hydrazine hydrate (4 µl ml^{-1}) at a constant stirring at a temperature of 95 °C. After that, 50 mg of $NiMn_2O_4$ nanoparticles were incorporated into rGO via ultrasonication for 2 h and then polymerization was performed by adding 115 µl and 37 µl of PSS and EDOT, respectively under vigorous stirring in ice bath. To this mixture, each of 0.05 M ammonium peroxydisulfate and ferric chloride in 30 ml solution was added slowly and stirred for 24 h in ice bath. The as obtained blue coloured solution indicates the successful polymerization of EDOT monomer in presence of $NiMn_2O_4$ nanoparticles and rGO nanosheets. Finally, the precipitate was washed and centrifuged with absolute ethanol and DI water and was kept in an oven at 60 °C. The block diagram for the synthesis of rGO/PEDOT:PSS/$NiMn_2O_4$ nanocomposite is shown in Figure 3.12.

3.4.3.1 Formation mechanism of rGO/PEDOT:PSS/$NiMn_2O_4$ nanocomposite

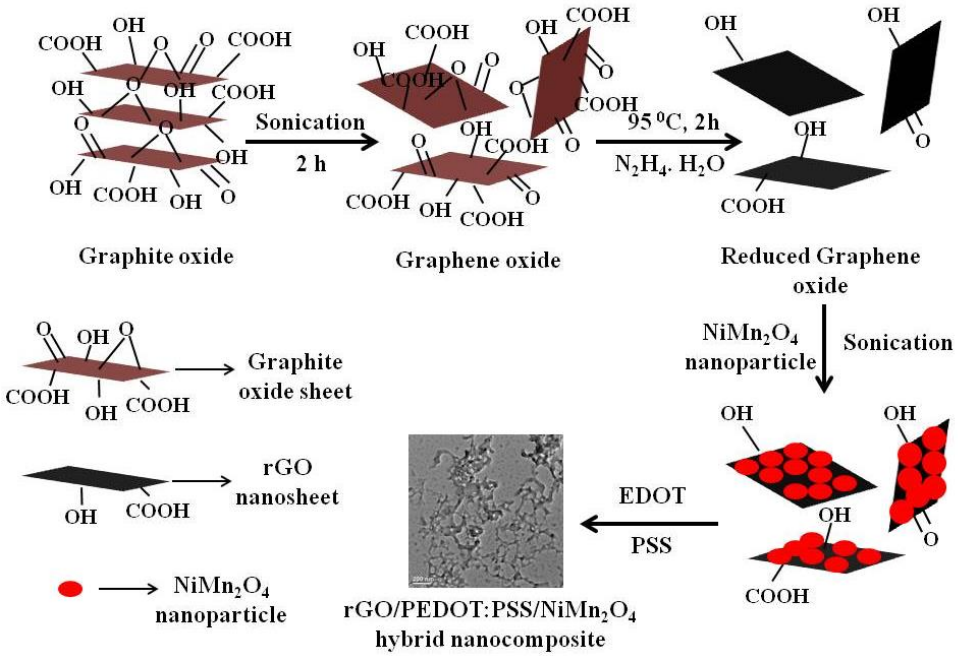

Figure 3.13: *Schematic illustration of the synthesis of rGO/PEDOT:PSS/$NiMn_2O_4$ nanocomposite.*

The schematic diagram of synthesizing rGO/PEDOT:PSS/$NiMn_2O_4$ nanocomposite is shown in Figure 3.13. Initially, the stacks of graphite oxide (GO) sheets have been separated by ultrasonication to form graphene oxide and then oxygen containing functional groups present on the edges and basal plane of graphene oxide sheets have been removed using hydrazine hydrate ($N_2H_4.H_2O$) that finally resulting in reduced graphene oxide (rGO) nanosheets. Solvothermally synthesized $NiMn_2O_4$ nanoparticles, dispersed within PEDOT:PSS matrix, are distributed over rGO nanosheets forming the porous network of rGO/PEDOT:PSS/$NiMn_2O_4$ nanocomposite.

3.5 Preparation of nanocomposite modified electrode

Prior to use, the indium tin oxide (ITO) glasses were cleaned by ultrasonication in DI water and absolute ethanol. To fabricate the working electrodes, the synthesized material (75%), carbon black (15%) and Nafion (10%) were dispersed together in ethanol solution and sonicated for 40 min to obtain a homogeneous mixture, followed by drop casting onto ITO glasses (1 cm × 1 cm) and dried in room temperature.

3.6 Characterization techniques

3.6.1 Scanning electron Microscopy

The scanning electron microscopy (SEM) is a powerful technique, which uses back scattered and secondary electrons to form an image rather than light. SEM is widely used for the analysis of surface of particles greater than 5 nm [13]. The magnification of SEM is about 250 times higher than the optical microscope. The reason behind the higher resolution is the use of electrons of much smaller wavelength [14]. The capability to differentiate two point objects of about equal intensity is known as resolution of the microscope. The electron column and control console are the main components of SEM [15]. The electron column comprises of an electron gun and two or more electromagnetic lenses that are used to focus the electron beam (0.2 keV to 40 keV) travelling down in an evacuated tube to form a thin probe (1-10 mm) [16]. In the electron column, the beam is deflected by pairs of scanning coils or pairs of deflector plates in the horizontal and vertical directions. The main aim of electron gun is to offer a stable beam of electrons. In thermionic electron guns, usually, tungsten is used due to its highest melting point and lowest vapour pressure among all metals. Since the spot size from a tungsten gun is considerably large to form a sharp image, hence electromagnetic lenses are used to

demagnify it and also to narrow it down that can scan over the surface of the object. The control console is made up of a cathode ray tube (CRT) viewing screen and computer to govern the electron beam. In this technique, a narrow electron beam is scanned over the sample and simultaneously, the produced signals are recorded that resulting into an image [17]. Different types of signals are produced upon impingement of electron beam on the specimen. Then the electron beam interacts with the sample producing a number of emissions such as secondary, back scattered and transmitted electrons along with X-ray radiation. SEM images are produced from the signals of secondary electrons and backscattered electrons. The electrons which elastically scatter at large angles (0^o to 180^o) due to interaction with the nucleus are called backscattered electrons. The intensity of the back-scattered electrons depends on the atomic number of the material. Distribution of different elements in the material can obtained from the images produced from the back-scattered electrons. Whereas, some electrons loss their kinetic energy during interaction with orbital shell electrons causing inelastic scattering. The electrons incident on the specimen may easily knock off loosely bound conduction electrons out of it. The scattered electrons are termed as secondary electrons that emit from the depth of 5 and 50 nm of the surface and give a clear image of the surface topography. In front of the detector, a positive voltage is applied to the collector to collect both secondary electron and backscattered electron signals. Only backscattered electrons are collected while secondary electrons are repelled upon application of negative voltage on the collector screen. Photomultipliers collect the electrons and amplify the electrical signals and feed to a cathode-ray tube for displaying the images [13]. If an inner shell electron is knocked off by the electron beam then an outer shell electron jumps to fill the vacant site of inner shell. In this process, the emitted electron is known as Auger electron. Apart from Auger electron, a photon of electromagnetic radiation can also be released by the ionized atom. The photon will be X-ray photon if energy released is sufficiently high. These photons are characteristic of the material and can be used analysis of elemental composition, which is known as Energy Dispersive analysis of X-rays (EDAX) [17]. The main advantage of SEM is that it gives a great amount of information regarding surface topology, morphology and composition [13], although it requires long scanning times to obtain high resolution. The sample should be conductive for SEM measurements to avoid charge build-up of the sample [13]. Therefore, platinum or gold particles are sputtered over the sample to form a conductive coating.

SEM analysis was done using a JEOL JSM 6390 LV model scanning electron microscope (shown in Figure 3.14) installed at department of Physics, Tezpur University, Assam, India. The images were taken at an accelerating voltage varying between 5-20 kV and magnification is fixed according to need from 3,000 X-20,000 X. Gold coating was done over the samples before SEM imaging and the samples were placed on carbon tape before viewing.

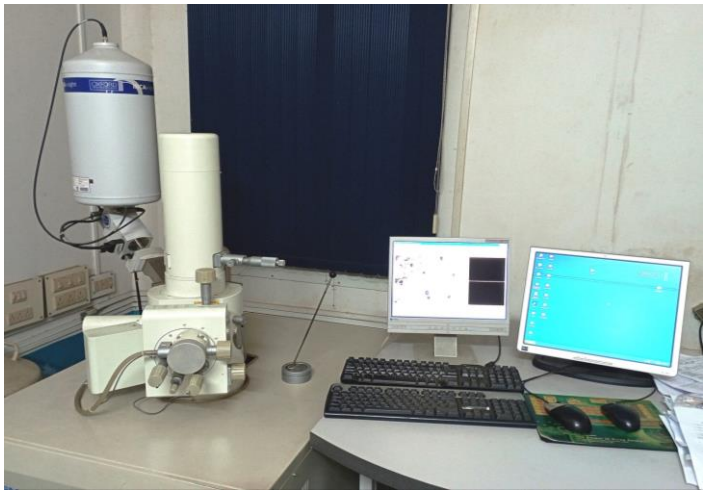

Figure 3.14: *Scanning electron microscope (JEOL, model JSM-6390 LV).*

3.6.2 High resolution transmission electron microscopy

High resolution transmission electron microscopy (HRTEM) is the premier and versatile technique used in the characterization of nanostructured systems to understand internal microstructure of materials. It gives direct visualization of structures and defects at a resolution of 0.1 nm. The main components of HRTEM include a vacuum system, an electron gun (to produce electron beam), electromagnetic lenses, specimen stage, apertures, imaging system and appendix. The technique involves [18]: (i) Electron gun, fitted with a tungsten filament cathode as the electron source, emits electron. The electron beam is accelerated by an anode usually at +100 keV (40 to 400 keV) with respect to the cathode. (ii) Illumination of electron occurs over a thin specimen in which the intensity of electron beam is uniform over the illuminated. Then the electron beam is diffracted by lattice of a crystalline or semi crystalline material and moved along different directions. (iii) This technique is related to the imaging and angular distribution analysis of the transmitted or forward scattered beam (unlike SEM where backscattered electrons are detected), which passes through a series of lenses. The information about the structure of specimen is carried by the electron beam that emerges from the specimen; which is

further magnified by the objective lens system of the microscope and focused onto an image capturing device, such as a fluorescent screen, on a layer of photographic film, or a CCD camera. The detected image can be displayed on a monitor or computer and (iv) energy analysis of the emitted X-rays. In a conventional transmission electron microscope, the incident electrons can interact with an object either by elastic scattering or inelastic scattering. In elastic scattering, path of incident electrons is changed without losing any energy while in inelastic scattering; there is energy loss due to interaction of incident electrons with the orbital electrons of an atom in the object. The electrons, which are hardly scattered, contribute positively to the image. However, the apertures in the optical path prevent the significantly deflected electrons from doing so resulting into differences in intensity of light that create the final image [19]. The imaging system comprises an objective lens and one or more projector lenses. The objective lens determines the degree of resolution in the image. The enlarged image of illuminated portion of the specimen is produced by this lens in a plane. The projector lens projects the final magnified image on the screen or photographic emulsion. Resolution and magnification of a microscope depends upon the wavelength and the energy of the radiation. Resolution increases with decrease in wavelength. Hence, resolution of TEM is higher than that of optical microscopy. An electron diffraction pattern known as Selected Area Electron Diffraction (SAED) can be obtained upon focussing an electron beam onto a small part i.e. several to hundreds of nanometers of the sample by adjusting the spot size [20]. The crystallinity of the specimen can be determined from the diffraction pattern. The image containing dots indicates single crystal while image consisting of a series of rings indicates that the specimen is amorphous.

The HRTEM images were obtained by using a high resolution transmission electron microscope (HRTEM) model JEM-2100 installed at Sophisticated Analytical Instrumentation Facility (SAIF), North-Eastern Hill University (NEHU), Shillong, Meghalaya, India shown in Figure 3.15 with an accelerating voltage of 200 kV. The samples for HRTEM experiments were prepared by dropping a small colloidal solution onto a coated copper-carbon grid and the excess solution was evaporated in ambient air at room temperature.

Figure 3.15: *High resolution transmission electron microscopy (JEOL, model JEM-2100).*

3.6.3 X-ray diffraction

X-ray diffraction (XRD) is a non-destructive analytical technique to analyse the physical and electronic structure of crystalline and non-crystalline materials. The X-rays are suitable to observe crystal size and disorder, structural parameters and atom positions in a crystalline solid due to comparable size of the wavelength of X-rays (~ 1 Å) to the size of atoms [21]. In the X-ray tube, electrons are generated by thermionic emission from tungsten filament on the application of approx. potential of 40 kV. Since high voltage is maintained across the electrodes, hence electrons are attracted towards the anode, which is a metal target, typically copper. The impingement of electrons on the copper target results into ejection of electrons from 1s orbital of copper. Therefore, 2p electrons jump to occupy the vacant site, consequently releasing their energy in the form of X-rays having a wavelength of 0.154056 nm [22]. These X-rays are collimated and directed into the sample. In X-ray diffraction technique, the electromagnetic waves interact with atoms of the crystal [21]. When a monochromatic X-ray beam falls on a crystalline material, the

incident X-ray photons interact with the electrons that surround the atoms. The electron clouds scatter X-rays in all directions. Fig. 3.16 represents the constructive interference of scattered waves.

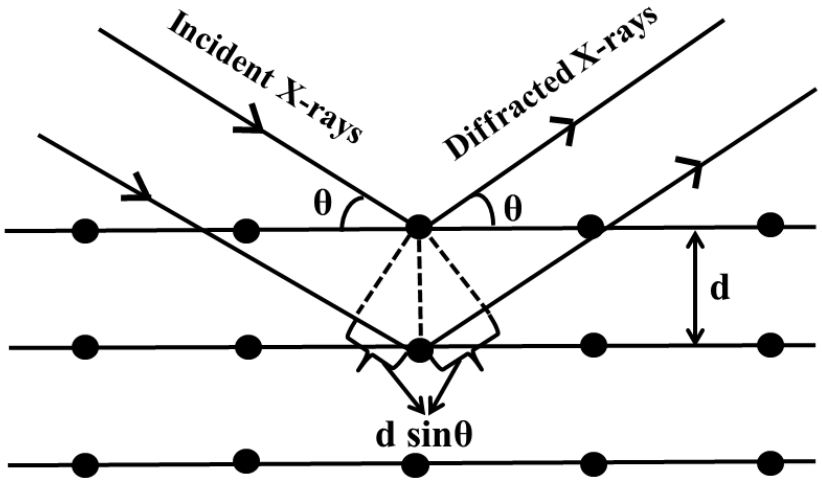

Figure 3.16: *Schematic representation of diffraction of X-rays by the crystal planes.*

X-ray diffraction patterns are plotted as the intensity of diffracted X-rays vs. angle 2θ. The crystal structure can be investigated using Bragg's law, in which constructive interference of two waves reflected from rows of atoms has been taken into consideration [17]. The XRD peaks appear at 2θ values at the condition of maximum constructive interference i.e. when Bragg's Law (equation 3.9) is satisfied [23].

$$n\lambda = 2d \sin\theta \qquad [3.9]$$

Where, n is the order of diffraction pattern, λ is the wavelength of incident X-rays, d is the interplanar spacing and θ is the incident angle.

XRD patterns arising due to interference of the X-ray beams reflected from atom cores, give information about crystal structure parameters such as crystallite size (domain length in case of amorphous polymers), d-spacing, diffraction planes, structure, phase and lattice constants etc.

The XRD patterns were obtained using a D8 Bruker AXS X-ray diffractometer (Germany) at Tezpur University, India as depicted in Figure 3.17. The measurements were performed using Cu K_α radiation having a wavelength of 1.5406 Å at 1^o min^{-1} scan rate.

Figure 3.17: *X-ray diffraction measurement unit (D8 Bruker AXS).*

3.6.4 Raman spectroscopy

Figure 3.18: *Photograph of Raman spectrometer (Renishaw in-via).*

Raman spectroscopy is a powerful technique to analyse structural characteristics of material at a local level. It is based on inelastic scattering of monochromatic light by matter, where the source of light is laser. In inelastic scattering, the frequency of photons in monochromatic light changes due to interaction with a sample. The information about the crystal structure and molecular vibrations can be obtained from Raman spectroscopy. Monochromatic light falls on the sample and the scattered light is examined by the

spectrometer. If the scattered photons have the same frequency as the incident photons, then the scattering process is called Rayleigh scattering, which is an elastic scattering and it occurs when light encounters molecules in air [24]. In Raman spectroscopy, the frequencies present in the radiation are observed to analyse the energy levels of molecules. During this process, (i) a photon is absorbed by the sample resulting into excitation of an electron from the ground to an excited state, (ii) a second photon induces the stimulated emission of a photon since the excited state transforms back to the ground state. The Raman scattering occurs if there is change in polarizability of the molecules. The incident photon energy can excite vibrational modes of the polarizable molecules, resulting into scattered photons with decrease in energy by the amount of vibrational transition energies. In Raman scattering, out of 10^7 of incident photons only about 1 photon collide the molecules, loss their energy, and scatter with a lower frequency resulting into Stokes lines in the spectrum of scattered radiation [14]. Stokes lines appear below Rayleigh scattering peak at the incident frequency. However, significant excitation of vibrational excited states of the scattering molecules, results into appearance of spectral line at frequencies above the incident frequency. These weaker lines are called anti-Stokes lines in the spectrum of scattered radiation. Raman Spectrometer comprises a Laser beam that passes through a sample filled narrow glass or quartz tube, light scatters sideways from the sample and then it is collected by a lens and passes into a grating monochromator. A sensitive photomultiplier tube (PMT) measures the signal and it is processed by a computer which plots the Raman spectrum after amplification. The Raman spectrum is plotted between the intensity of the scattered light versus the shift in wave number from the original laser line. Each of the characteristic peaks in a Raman spectrum signifies a certain molecular or lattice vibration [25]. The position of the peak is associated with mode of vibration of a particular functional group present in the sample. Therefore, Raman spectrum gives the molecular fingerprint of the sample.

Raman measurements were carried out using a Renishaw inVia spectrometer (Renishaw, Wotton-under-Edge, UK) as shown in Figure 3.18 equipped with 514.5 nm argon ion laser at an incident power of 5 mW within the range of 500-3000 cm^{-1}.

3.6.5 X-ray photoelectron spectroscopy

X-ray photoelectron spectroscopy (XPS) is a quantitative spectroscopic technique that gives information on the elemental composition, empirical formula, chemical state, electronic state of the elements within a material and the distribution of these elements

across the surface. It is a surface-sensitive technique since it can detect those electrons that are generated on the surface of the specimen i.e. typical probing depth is upto only 10 nm [26]. This technique is based on the photoelectric effect, whereby a material is irradiated by a beam of aluminium or magnesium X-rays of sufficient energy and the kinetic energy and number of photoelectrons that escape from the top 10 nm of the surface are measured simultaneously. Since the energy of a particular X-ray wavelength is known, hence the binding energy of each of the emitted electrons can be obtained using the following equation [26]:

$$E_{binding} = E_{kinetic} - E_{photon} - \varphi \qquad [3.10]$$

Where $E_{binding}$ is the energy of emitted electron, E_{photon} is the energy of X-ray photons, $E_{kinetic}$ is the kinetic energy of emitted electron and ϕ is the work function of spectrometer. The elements present in the material can be identified from the binding energies of the characteristic peaks. The binding energy depends upon the atomic number of the atom. Generally, binding energy of the core electrons decreases with increase in charge of an atom [27]. Hence, the composition of surface and the chemical state of the material can be identified if binding energy is known. The binding energy also depends upon oxidation state of the atom. The variation of oxidation state of the atom causes change in binding energy which is measured by XPS and known as chemical shift. By applying appropriate sensitivity factors to the peak areas, one can calculate the composition of each element. Except hydrogen and helium, the elements of periodic table with an atomic number between those of lithium and lawrencium can be detected [28]. The detection limit may be upto parts per million (ppm) with a very long collection time. When monochromatic X-ray beam strikes the sample it penetrates through a few nanometers and the emitted electrons enter into the analyzer through a set of electrostatic and magnetic lenses [28].

Besides photoelectrons, there are also possibilities of emission of Auger electrons. When an electron from the outer orbital jumps into the vacancy created by the incident photoelectron in the core level, then simultaneously another electron having kinetic energy equal to the difference in the energies of the two orbitals, is generated, known as Auger electron. Both photoelectrons and Auger electrons are included in the detected electrons, which are used to identify the element and the oxidation state. The kinetic energy of photoelectron depends upon the X-ray source, while the energy of Auger electrons is independent of it i.e. the position of peaks associated with the photoelectrons varies with X-ray; however the position of Auger peak remains same irrespective of the source used.

XPS measurements were carried out using ESCALAB Xi + (Thermo Fisher Scientific Pvt. Ltd., UK) installed at CSIR-North East Institute Of Science And Technology (NEIST), Jorhat as shown in Figure 3.19, using a monochromatic aluminium Kα radiation in a vacuum of 10^{-10} mbar. The pass energy of the analyzer was kept constant at 20 eV for all scans.

Figure 3.19: *Photograph of X-ray photoelectron spectrometer (ESCALAB Xi +).*

3.6.6 N_2 adsorption-desorption measurements

Figure 3.20: *Set-up used for Nitrogen adsorption-desorption measurements (Quantachrome, model NOVA 1000E).*

Low-pressure N_2 gas adsorption method is used for the measurement of adsorption and desorption isotherms of nitrogen at the boiling point of liquid nitrogen i.e. 77.3 K at 730 mm Hg pressure and to characterize the pore structure of material [29, 30]. The adsorption and desorption isotherms are plotted over a relative pressure (P/P_o) range of 0.05 to 0.99 at a constant temperature. In this experiment, the pressure is increased upto condensation pressure in adsorption branch and then reduced from P_o i.e. the saturation pressure in desorption branch. The gas adsorption isotherm is plotted as the quantity of gas adsorbed. The sample chamber is evacuated of all gas at 120-200 ^oC cooled to a temperature of 77 K, *i.e.* the temperature of liquid nitrogen. A known quantity of N_2 is introduced into the sample chamber and the pressure of nitrogen is increased gradually. Then nitrogen gas is adsorbed on the surface of the sample causing decrease in pressure until an equilibrium pressure is reached [31]. The equilibrium pressure and the quantity of adsorbed nitrogen gas at each equilibrium temperature are noted. During adsorption process, there is gradual increase in the pressure of nitrogen over the sample until near saturation pressure is obtained. Subsequently, in desorption process, the step-wise decrease in pressure occurs until the pressure reaches to its initial value. The nitrogen adsorption-desorption isotherms are plotted as quantity of the volume of nitrogen gas adsorbed and desorbed along Y-axis versus relative pressure (P/Po) along X-axis.

Nitrogen adsorption-desorption measurements were carried out using Quantachrome (NOVA 1000E) analyzer (Figure 3.20) at liquid nitrogen temperature of 77 K. The specific surface areas of the samples were obtained by Brunauer-Emmett-Teller (BET) method from the adsorption data while the pore volume and pore size distribution were determined from the desorption data using the Barrett-Joyner-Halenda (BJH) method.

3.7 Measurements of electrochemical properties

Electrochemical measurements were performed on a potentiostat/galvanostat (Autolab PGSTAT 302N, Metrohm, Netherlands) equipped with NOVA software in a standard three electrode system as shown in Figure 3.21. The working electrode was electrocatalyst modified indium tin oxide (ITO) electrode. Ag/AgCl (3M KCl) and Platinum (Pt) wire were used as reference and counter electrodes, respectively. The electrochemical measurements were carried out in 0.5 M NaOH electrolyte. All the solutions were bubbled through pure nitrogen for 15 mins before each experiment.

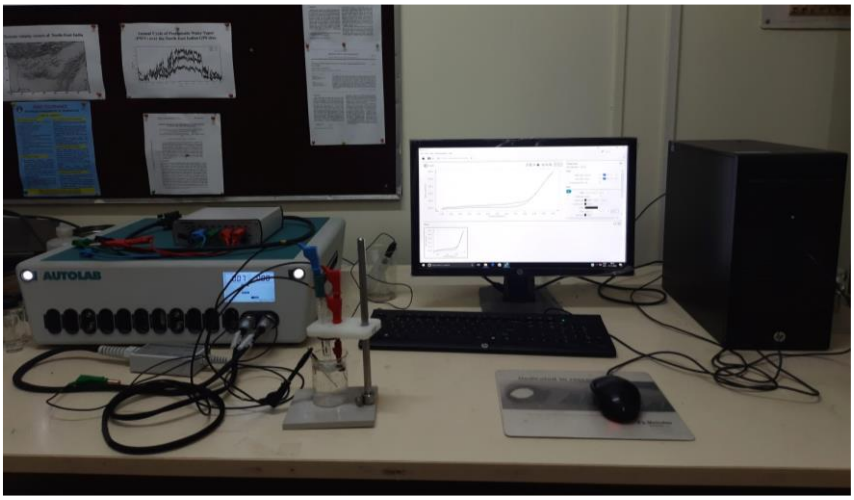

Figure 3.21: *Photograph of potentiostat/galvanostat (Autolab PGSTAT 302N, Metrohm, Netherlands).*

3.7.1 Cyclic voltammetry

Cyclic voltammetry (CV) is used to understand the electrochemical processes and charge transfer kinetics at the electrode. CV was done to observe electrochemical behaviour of the modified ITO electrodes in presence of 0.5 M NaOH electrolyte. The oxidation of methanol was investigated at working electrodes by sweeping at a scan rate of 50 mV s^{-1} in 0.5 M methanol containing in 0.5 M NaOH electrolyte. CV was also performed by varying the scan rate and concentration of methanol to analyse the methanol oxidation process.

3.7.2 Linear sweep voltammetry

In linear sweep voltammetry (LSV), the current is measured at working electrode whereas the linear potential is swept between the reference electrode and working electrode. The peak current at a certain potential indicates the reduction or oxidation of species. It depends on rate of electron transfer, chemical reactivity of electroactive species and the voltage scan rate [32]. LSV was carried out with 0.5 M methanol containing in 0.5 M NaOH electrolyte at a scan rate 1 mV s^{-1}.

3.7.3 Electrochemical impedance spectroscopy

Electrochemical Impedance spectroscopy (EIS) is a powerful tool to understand the electrical properties of electrodes and interfaces [32]. It is also used to study the formation of electric double layer, transfer of charge at electrode-electrolyte interface, charge transport kinetics in electrode materials, dielectric behaviour of electrodes and electrolyte [32]. EIS measurement was conducted in a frequency range from 0.1 Hz to 10 MHz with constant amplitude of 10 mV under potentiostatic mode.

3.7.4 Chronoamperometry

Chronoamperometry is an important electrochemical technique, where the response of a working electrode is measured over a period of time to check the stability. In this technique, the current response of the catalyst is measured by holding a constant potential between the working electrode and the reference/counter electrode over a period of time [33]. Stability of the catalyst depends on its ability to continue the reaction for a long duration [33]. The stability of the working electrodes was evaluated from the chronoamperograms recorded at a certain potential versus that of Ag/AgCl for 3600 s.

3.7.5 Cyclic stability study

Cyclic stability test was done to determine cycle life of the electrode. The cycle life was obtained by calculating current retention of the modified electrode for 1000 cycles. The current retention is calculated from the current density values of 1^{st} and 1000^{th} CV cycles. Cyclic voltammograms of the modified ITO electrodes were recorded in 0.5 M methanol containing in 0.5 M NaOH electrolyte at a scan rate of 50 mV s^{-1} for 1000 cycles. After 1000 CV cycles, the electrolyte was replaced with fresh electrolyte and again CV was recorded.

3.8 References

[1] Marcano, D.C., Kosynkin, D.V., Berlin, J.M., Sinitskii, A., Sun, Z., Slesarev, A., Alemany, L.B., Lu, W. and Tour, J.M. Improved synthesis of graphene oxide. *ACS nano*, 4(8):4806-4814, 2010

[2] Hareesh, K., Shateesh, B., Joshi, R.P., Williams, J.F., Phase, D.M., Haram, S.K. and Dhole, S.D. Ultra high stable supercapacitance performance of conducting polymer coated MnO_2 nanorods/rGO nanocomposites. *RSC advances*, 7(32):20027-20036, 2017.

[3] Wang, H., Lu, Z., Qian, D., Li, Y. and Zhang, W. Single-crystal α-MnO_2 nanorods: synthesis and electrochemical properties. *Nanotechnology*, 18(11):115616, 2007.

[4] Han, G., Liu, Y., Zhang, L., Kan, E., Zhang, S., Tang, J. and Tang, W. MnO_2 nanorods intercalating graphene oxide/polyaniline ternary composites for robust high-performance supercapacitors. *Scientific reports*, 4(1):1-7, 2014.

[5] Mu, B., Zhang, W., Shao, S. and Wang, A. Glycol assisted synthesis of graphene-MnO_2-polyaniline ternary composites for high performance supercapacitor electrodes. *Physical Chemistry Chemical Physics*, 16(17):7872-7880, 2014.

[6] Nakate, U.T., Lee, G.H., Ahmad, R., Patil, P., Bhopate, D.P., Hahn, Y.B., Yu, Y.T. and Suh, E.K. Hydrothermal synthesis of p-type nanocrystalline NiO nanoplates for high response and low concentration hydrogen gas sensor application. *Ceramics International*, 44(13):15721-15729, 2018.

[7] Kumar, J.P., Giri, S.D. and Sarkar, A. Mesoporous NiO with different morphology: Synthesis, characterization and their evaluation for oxygen evolution reaction. *International Journal of Hydrogen Energy*, 43(33):15639-15649, 2018.

[8] Dong, L., Chu, Y. and Sun, W. Controllable synthesis of nickel hydroxide and porous nickel oxide nanostructures with different morphologies. *Chemistry-A European Journal*, 14(16):5064-5072, 2008.

[9] Nadargi, D.Y., Tamboli, M.S., Patil, S.S., Mulla, I.S. and Suryavanshi, S.S. Development of Ag/ZnO nanorods and nanoplates at low hydrothermal temperature and time for acetone sensing application: an insight into spillover mechanism. *SN Applied Sciences*, 1(12):1-10, 2019.

[10] Chen, J., Yao, B., Li, C. and Shi, G. An improved Hummers method for eco-friendly synthesis of graphene oxide. *Carbon*, 64:225-229, 2013.

[11] Umeshbabu, E. and Rao, G.R. $NiCo_2O_4$ hexagonal nanoplates anchored on reduced graphene oxide sheets with enhanced electrocatalytic activity and stability for methanol and water oxidation. *Electrochimica Acta*, 213:717-729, 2016.

[12] Ding, R., Qi, L., Jia, M. and Wang, H., Porous $NiCo_2O_4$ nanostructures as bi-functional electrocatalysts for CH_3OH oxidation reaction and H_2O_2 reduction reaction. *Electrochimica Acta*, 113:290-301, 2013.

[13] Klabunde, K.J. and Sergeev, G.B. *Nanochemistry*. Newnes, 2nd edition, 2013.

[14] Sulaiman, Y. *Characterisation of PEDOT and its derivatives in electrochemical sensing applications*. PhD thesis, Department of Chemistry, Durham University, 2012.

[15] Lawes, G. *Scanning electron microscopy and X-ray microanalysis*. United State, 1987.

[16] Kaufmann, E. N. *Characterization of Materials*, John Wiley & Sons, Inc., Hoboken, New Jersey, 2003.

[17] Oko, D.N. *Electrocatalytic Activity of Small Organic Molecules at PtAu Alloy Nanoparticles for Fuel Cells and Electrochemical Biosensing Applications.* PhD thesis, Université du Québec, Institut national de la recherche scientifique, 2014.

[18] Hassan, K.T. *Synthesis of aerogels, nanocomposites and lightweight silica aerogel superinsulation Nano composites.* PhD thesis, School of Engineering, Newcastle University, UK, 2019.

[19] Kumari, S. *Synthesis, functionalization and catalytic application of porous hybrid materials*. PhD thesis, Chemical Engineering and Process Development Division, CSIR-National Chemical Laboratory, India, 2015.

[20] Ren, Y. *Applications of ordered mesoporous metal oxides: energy storage, adsorption, and catalysis.* PhD thesis, School of Chemistry, University of St Andrews, 2010.

[21] Sayeed, M.A. *Electrochemical fabrication of nanostructured metal oxides for the oxygen evolution reaction.* PhD thesis, School of Chemistry, Physics and Mechanical Engineering, Queensland University of Technology, 2018.

[22] Björk, E.M. *Mesoporous Building Blocks: Synthesis and Characterization of Mesoporous Silica Particles and Films*. PhD thesis, Department of Physics, Chemistry and Biology, Linköping University Electronic Press, 2013.

[23] Bunaciu, A.A., UdriŞTioiu, E.G. and Aboul-Enein, H.Y. X-ray diffraction: instrumentation and applications. *Critical reviews in analytical chemistry*, 45(4):289-299, 2015.

[24] Banwell, C.N. and McCash, E.M. *A Book: Fundamentals of Molecular Spectroscopy*. McGraw Hill Education, 2002.

[25] Vašková, H. A powerful tool for material identification: Raman spectroscopy. *Int. J. Math. Model. Methods Appl. Sci*, 5:1205-1212, 2011.

[26] Van der Heide, P. *X-ray photoelectron spectroscopy: an introduction to principles and practices*. John Wiley & Sons, 2011.

[27] Chastain, J. and King Jr, R.C. *Handbook of X-ray photoelectron spectroscopy*. Perkin-Elmer Corporation, 1992.

[28] Roger Barba, I. *Investigations into electrochemical water splitting*, PhD thesis, School of Chemistry, University of Glasgow, 2017.

[29] Anovitz, L.M. and Cole, D.R. Characterization and analysis of porosity and pore structures. *Reviews in Mineralogy and geochemistry*, 80(1):61-164, 2015.

[30] Lawrence, M. and Jiang, Y. Porosity, pore size distribution, micro-structure. In *Bio-aggregates based building materials*, pages 39-71, ISBN:978-94-024-1030-3. Springer, Dordrecht, 2017.

[31] Sinha, P., Datar, A., Jeong, C., Deng, X., Chung, Y.G. and Lin, L.C. Surface area determination of porous materials using the Brunauer-Emmett-Teller (BET) method: limitations and improvements. *The Journal of Physical Chemistry C*, 123(33):20195-20209, 2019.

[32] Wijeratne, K. *Conducting Polymer Electrodes for Thermogalvanic Cells*. PhD thesis, Department of Science and Technology, Linköping University Electronic Press, 2019.

[33] Rezaei, B. and Irannejad, N. Electrochemical detection techniques in biosensor applications. In *Electrochemical biosensors*, pages 11-43, ISBN:9780128164914. Elsevier, 2019.